Characterizing chaotic dispersion in a coastal tidal model

Steinar Orre[1] *, Bjørn Gjevik[2], Joseph H. LaCasce[3]

[1]*Nansen Environmental and Remote Sensing Center & Bjerknes Centre for Climate Research, Bergen, Norway*

[2]*Department of Mathematics, University of Oslo, Oslo, Norway*

[3]*Norwegian Meteorological Institute, Oslo, Norway*

Abstract

Diverse Lagrangian methods are used to study dispersion and mixing in a model in the Norwegian Trondheim fjord. We focus on the tidally-driven currents, neglecting wind-forcing, and generate a large number of particle trajectories. We first consider traditional measures (absolute and relative dispersion) involving averages over all particles. We then contour those measures, to gauge the spatial variations. Then we examine a more recently developed measure, the Direct Lyapunov Exponent (DLE), to further refine the description of the spatial variability. The results suggest regions of strong mixing adjacent to regions with weak mixing, so that particles in nearby regions may experience very distinct evolutions. And M_2 dominates the dispersion; adding additional tidal components affects mainly the amplitude of the particle excursions rather than the character of the mixing.

Key words: Chaotic dispersion, Dynamical Systems, Direct Lyapunov Exponents, Norwegian coast, tidal currents

1 Introduction

The coastal shelf is an important region for shipping and oil exploration, for fishing and aquaculture, and for recreation. As such, the transport of waterborne nutrients, sediments and pollutants in the coastal environment is of vital interest. Changes in sewer outflow can impact recreational activities and an oil

* corresponding author

Email address: steinar.orre@nersc.no (Steinar Orre[1]).

spill can significantly affect fish stocks. So accurate assessments of transport in given regions is highly desirable.

Trondheimsleia and the Trondheim fjord on the western coast of Norway are such regions, used extensively by fishing and shipping companies and for various industrial development projects. The flow in the fjord is complex, due to its irregular coasts and variable bathymetry, and this hinders simple characterizations of the mixing. It is difficult to sample directly the diverse currents present here, but numerical models are becoming sophisticated enough to provide realistic predictions. Models can also be used for simulating pollutant transport and also determining which physical processes most affect that transport.

Hereafter we focus on one portion of the mixing in the Trondheim fjord, that due to the tides. This is a natural place to start, since tides dominate the wind-driven currents in terms of flushing (Orre, 2004). We use a high resolution (50 m) model to advect a large number of passive particles, and then use the resulting trajectories to diagnose the mixing. We do this by using various Lagrangian measures, some traditional and some developed recently. The picture which emerges is surprisingly complex.

Tidal mixing has been studied extensively, (e.g. Bowden, 1965; Forrest and Usseglio-Polatera, 1984; Geyer and Signell, 1992; Signell and Butman, 1992; Ridderinkhof and Zimmerman, 1992; Gjevik, 1996). Spatial variations in the flow, induced primarily by topography, permit particles to drift systematically rather than just periodically returning to their starting positions. If the horizontal particle displacements are comparable to the scale of the spatial variations (e.g. between major topographic features), the particle trajectories can even be unpredictable. This can lead to efficient lateral mixing of material.

Much of the early work on Lagrangian dynamics was motivated by the theory of turbulence. The emphasis was on Lagrangian statistics, prioritizing the *probability* of particle displacements rather than describing single trajectories.[1] Given that the early theoretical work concerned homogeneous turbulence, the statistics involved averaging over particle trajectories from the whole flow. Single trajectories were viewed as irreproducible, and only the average behavior was thought to be robust. But such averages ignore the spatial variations in mixing which occur in most realistic environments. So more recent work, much of it motivated by chaos and dynamical systems theory (Ottino, 1990; Wiggins, 1992), has sought to understand these variations.

Lagrangian chaos, in which particle trajectories depend sensitively on their starting positions and times, can occur in the simplest of flows. A seminal example is the "blinking vortices" of Aref (1984). In this, two co-rotating vor-

[1] Discussions of Lagrangian statistics are given by Batchelor (1953), Bennett (1987) and LaCasce and Ohlmann (2003).

tices are alternately turned on and off, advecting particles around them. The Eulerian flow is entirely deterministic and can be expressed by a mathematical mapping. But the Lagrangian motion can be chaotic, the more so with large amplitude forcing. This example is relevant to mixing due to tides, which is also oscillatory. Ridderinkhof and Zimmerman (1992) examined tidal dispersion from the perspective of chaotic mixing in relation to the Dutch Wadden Sea, as did Ridderinkhof and Ridderinkhof and Loder (1994) for tidal flow in the Gulf of Maine.

More recently, dynamical systems theory has sought to characterize the structures in chaotic flow which contribute to mixing. There are, for example, hyperbolic (saddle) points near which particle pair separations grow exponentially in time. There are "manifolds", distinct material surfaces along which particle separations contract or grow exponentially (e.g. Wiggins, 2005). There are also transport *barriers*, across which particle motion is severely hindered or prevented (e.g. Boffetta et al., 2001). A barrier surrounds the polar vortex in the southern hemisphere stratosphere and hinders the lateral spread of ozone (e.g. Haynes, 2005).

Hereafter we consider the tidal mixing in Trondheimsleia and the Trondheim fjord using various measures from turbulence and dynamical systems theories. For this study we focus solely on mixing induced by one or more of the dominant tidal components, and exclude wind forcing and nonlinear effects. The model is described in section 2 and the methods described in Section 3. The results from two important regions in the fjord are presented in section 4 and we conclude with discussion in section 5.

2 The high resolution tidal model

Moe et al. (2003), present a numerical model for simulating tides on a section of the shelf off the coast of Møre and Trøndelag in Mid-Norway. This model, which has 500 m grid resolution, demonstrated considerable skill in estimating both the tidal velocity and elevation fields. The model is based on the (depth-integrated) shallow water equations with linearized advection terms:

$$\begin{aligned} \frac{\partial \eta}{\partial t} &= -\frac{\partial U}{\partial x} - \frac{\partial V}{\partial y} \\ \frac{\partial U}{\partial t} - fV &= -gH\frac{\partial \eta}{\partial x} - c_D\frac{\sqrt{U^2+V^2}}{H}\frac{U}{H} \\ \frac{\partial V}{\partial t} + fU &= -gH\frac{\partial \eta}{\partial y} - c_D\frac{\sqrt{U^2+V^2}}{H}\frac{V}{H} \end{aligned} \tag{1}$$

where (U, V) specify the volume fluxes per unit length in the horizontal plane,

η is the vertical displacement of the sea surface from the mean sea level, $H = H_0 + \eta$ the total depth, H_0 the mean depth, g acceleration of gravity, f the Coriolis parameter, and c_D the drag coefficient of the quadratic bottom shear stress. The depth-averaged velocity is then given by:

$$\overline{u} = \frac{U}{H} \quad , \quad \overline{v} = \frac{V}{H}. \tag{2}$$

The model employs realistic topography, but with a 2 m wall at the coasts. The slip boundary condition is used at the wall. [2]

The 500 m model was then used by Gjevik et al. (2005) to determine the flow conditions along the open boundaries for a high resolution model for the inner coastal region. The domain of the latter is depicted in Figure 1. The depth matrix was calculated for an UTM coordinate grid (with $\Delta x = \Delta y = 50$ m) based on multibeam bathymetric soundings and high resolution hydrographic surveys by the Norwegian Hydrographic Service. With a horizontal Cartesian coordinate system, origin at left lower corner of figure (1), and x- and y-axis along the model domain, the horizontal components of the tidal depth mean current velocity are represented as

$$\begin{aligned} u(x,y,t) &= \sum_i \overline{u}_i \cos(\omega_i t + \chi_i - \delta_{ui}), \\ v(x,y,t) &= \sum_i \overline{v}_i \cos(\omega_i t + \chi_i - \delta_{vi}). \end{aligned} \tag{3}$$

Here, (u_i, v_i) denotes the amplitude of the depth mean current of the i-th tidal constituent, $(\delta_{ui}, \delta_{vi})$ is the Greenwich phase, ω_i the angular velocity and χ_i the astronomical argument.

Simulations for the coasts of Møre and Trøndelag yielded harmonic constants for the semi-diurnal components M_2, S_2, N_2 and the largest diurnal component, K_1. Hereafter, we focus on the dispersion induced solely by these tidal components. We therefore neglect the effects of wind forcing and nonlinearities. As stated, the tides dominate the wind-forced currents in the region, nevertheless it is possible that low frequency fluctuations induced by the wind could modify the tidal dispersion; that will be studied later on. Nonlinear effects are excluded (apart from the quadratic bottom stress) because advection has not yet been implemented in the model. So we exclude overharmonic tides, like the M_4, and the tidal residual flow. Both have a negligible effect in the deeper parts of the channels, which cover most of the domain, but could modify the response in the shallows (where bottom friction will also be proportionally greater). Their effects will also be studied later on.

[2] The lateral boundary layer plays a much smaller role in the basin than the bottom boundary layer, noted also for instance by Signell and Geyer (1991).

Since the model employs the shallow water equations, it does not capture vertical shear. The region is often well-mixed, particularly in winter, with little vertical shear. But shear does become important in certain regions and in the summer season. The focus hereafter is on the surface dispersion, but because of the lack of shear, the subsurface dispersion could potentially differ.

2.1 Lagrangian particles

The model was used to advect passive (massless) Lagrangian particles. Their trajectories were calculated by numerical integration of the equations

$$\frac{dx_k}{dt} = u(x_k, y_k, t) \quad , \quad \frac{dy_k}{dt} = v(x_k, y_k, t), \tag{4}$$

where subscript k denotes the number of single particles ($k = 1, ..., M, M =$ number of particles) and (x_k, y_k) the position of particle k.

For the numerical integrations we used a fourth-order Runge-Kutta scheme as an initiator combined with a fourth-order Adams-Moulton scheme. This combination reduces computational cost while yielding a truncation error $\propto \Delta t^4$. In practice, however, we usually say that a fourth-order numerical integration scheme has a second-order accuracy (Vetterling and Flannery, 2002). The code for integrating these equations was developed by Gjevik (1996), and further modified by Ommundsen (2002).

3 Method

3.1 Lagrangian statistics

Here we consider analyzing particle trajectories generated by the model. First we examine probabilistic measures, which reflect how particles behave as a group. These are of two types, measures concerning single particles and those involving multiple particles.

Central to single particle statistics are the mean and variance of particle displacements which reflect, respectively, the drift and spread of a "cloud" of tracers. The variance is referred to as the "absolute dispersion", defined:

$$D^2(t) = \sum_i (x_i(t) - x_i(0))^2 + (y_i(t) - y_i(0))^2 \tag{5}$$

where the sum is over all particles. The time derivative of the dispersion is called the "diffusivity". Under fairly general conditions (Taylor, 1921), the diffusivity grows linearly in time for particles near their starting positions and is constant at later times, the latter being a signature of Brownian motion. So the absolute dispersion increases quadratically in time initially and linearly later on. Between the asymptotic limits, one occasionally observes an intermediate growth phase, known as anomalous diffusion (Young, 1999). Anomalous diffusion has been found in experiments (e.g. Solomon et al., 1993) but has been difficult to resolve in geophysical flows.

The joint statistics of multiple particles reflect the straining out of a tracer cloud. A central quantity is the variance of two particle separations, defined as "relative dispersion":

$$R^2(t) = \sum_{i \neq j} (x_i(t) - x_j(t))^2 + (y_i(t) - y_j(t))^2 \ . \tag{6}$$

Relative dispersion exhibits similar small and large time asymptotic behavior as the absolute dispersion. At late times (large separations), the velocities of the particle pair are uncorrelated and relative dispersion becomes absolute. But relative dispersion exhibits a wealth of intermediate time behavior which, depending on the initial particle separations, can persist for long periods. In addition, this intermediate behavior depends on the flow. Lagrangian chaos causes relative dispersion to grow exponentially while dispersion exhibits a power law dependence on time in the (3-D) turbulent inertial range. Excellent reviews of relative dispersion are given by Bennett (1987) and Sawford (2001); a recent discussion of Lagrangian statistics in relation to observations is given by LaCasce (2005).

3.2 Dynamical Systems Theory

Because Lagrangian statistics involve averages over many particles, they neglect flow inhomogeneities. Particles near energetic features, like vortices, are averaged together with others in quiescent regions. More recent measures address inhomogeneity by seeking to identify flow structures which dominate the particle spreading. To consider these, it is useful to define a *flow map*:

$$\mathcal{F}^t \ : \ \mathbf{x}_0 \mapsto \mathbf{x}(t_0 + t), \tag{7}$$

where $\mathcal{F}$ relates a set of particle positions at time t_0 to their later positions at time $t_0 + t$. If the flow is periodic in time and t is the period, (7) is called a Poincare or a *first return* map. For numerically generated flows the velocity is

known only at discrete spatial and temporal points. The flow (7) then defines a sequence of mappings, $\mathcal{F}^n(\mathbf{x}_0) = \mathbf{x}_n$, where n labels the discrete time.

There are special features in the flow, called "fixed points", under such a mapping. These are points, $\mathbf{p}$ such that $\mathbf{p} = \mathcal{F}^n(\mathbf{p})$ for every n. We may further distinguish "hyperbolic" and "elliptic" fixed points. The latter occur, for instance, at vortex centers and cause particle pair separations to grow algebraically in time. Hyperbolic points produce exponential growth of pair separations. Associated with hyperbolic points are "manifolds", distinct material surfaces along which particle separations contract ("stable manifolds") or grow ("unstable manifolds") exponentially. In terms of the mapping, the stable manifold $W^s(\mathbf{p})$ of a hyperbolic point $\mathbf{p}$ consists of all points $\mathbf{x} \in \mathbf{R}^2$ such that $\mathcal{F}^t(\mathbf{x}) \to \mathbf{p}$ as $t \to \infty$ and the unstable manifold $W^u(\mathbf{p})$ is the set of all points $\mathbf{x} \in \mathbf{R}^2$ such that $\mathcal{F}^t(\mathbf{x}) \to \mathbf{p}$ as $t \to -\infty$. The result is that stable manifolds act as attracting material surfaces and unstable manifolds as repelling surfaces.

Different measures have been developed for detecting fixed points and manifolds (e.g. Wiggins, 1992; Malhotra and Wiggins, 1998; Wiggins, 2005). These were originally designed for idealized flows, such as kinematic models with periodic time dependence. Examples of such studies in the oceanic context include the mixing near an idealized meandering jet (Miller et al., 1997; Rogerson et al., 1999) and in a recirculation behind an island (Miller et al., 2002).

3.3 Lyapunov exponents

Detecting fixed points and manifolds is less straightforward in realistic velocity fields. Nevertheless it is still possible to identify structures which dominate straining, by looking directly at particle displacements. Several of these methods are centered on the concept of a *Lyapunov exponent*. Consider a pair of trajectories near a hyperbolic point with initial displacement $r(0)$. The relative separation between them will grow exponentially fast with time;

$$r(t) \simeq r(0)e^{\lambda t}, \tag{8}$$

where λ is a parameter with dimension t^{-1}. For steady or periodic flows (to which the concept of an infinite time limit applies), λ corresponds to a Lyapunov exponent. Most flows however are non-periodic and most experiments of finite length, so one speaks of a "Finite Time Lyapunov Exponent" (FTLE), defined:

$$\lambda(\tau) = \lim_{r(0)\to 0} \frac{1}{\tau} \ln \frac{r(\tau)}{r(0)}, \tag{9}$$

assuming an infinitesimally small initial displacement. Under exponential growth, the FTLE for a particle pair is constant in time. FTLEs have been used to

gauge mixing in kinematic models (Pierrehumbert, 1991), in models of the stratosphere (Shepherd et al., 2000), in 2-D turbulence (Lapeyre, 2002) and with in situ data from the ocean surface (LaCasce and Ohlmann, 2003).

In inhomogeneous flows, different particle pairs exhibit different growth rates (pairs near elliptic points have Lyapunov exponents of zero). However if one has an array of initially equally-spaced particles, one can map out the Lyapunov exponent field by using information from the trajectories. To do this, we define a Cauchy-Green strain tensor;

$$\Sigma_t(\mathbf{x}_0) = \left[\frac{\partial \mathbf{x}}{\partial \mathbf{x}_0} \right]^T \left[\frac{\partial \mathbf{x}}{\partial \mathbf{x}_0} \right], \tag{10}$$

where $\mathbf{x}_0$ is the initial position vector, and $\mathbf{x}$ the position after being advected by the velocity field over timestep t. Four neighboring trajectories can be used to compute the finite differences in the strain tensor (10). Then the growth rate in equation (9) is replaced by the the square root of the maximum eigenvalue σ_t of the strain tensor (10), an indicator of the maximum stretching rate. One may then define the *Direct Lyapunov Exponent*:

$$\mathrm{DLE}_t(\mathbf{x}_0) = \frac{1}{t - t_0} \ln \sqrt{\sigma_t(\mathbf{x}_0)} = \frac{1}{2(t - t_0)} \ln \sigma_t(\mathbf{x}_0). \tag{11}$$

Note the DLE is a function of space. Contour plots of the DLE reveal regions of heightened stretching, which generally are associated with hyperbolic invariant manifolds (Haller and Yuan, 2000; Haller, 2001).

4 Results

The model domain is shown in Figure 1. In investigating the dispersion properties, we will focus initially on the M_2 tide, the most energetic component. The effect of adding additional components is considered afterward.

We will also focus on two sub-regions, shown in Figures 2 and 3. These exhibit the strongest tidal currents in the fjord and thus should experience the greatest mixing. Each covers an area 8×8 km. The region in Figure 2 includes the narrow channel between Garten and Storfosna in Trondheimsleia. The large tidal velocities here occur primarily on the shallow banks and are clearly topographically constrained. The region in Figure 3 includes the inner region of Trondheimsleia and the mouth of the Trondheim fjord. Here too the currents follow the topography, especially off the northern tip of Agdenes and on the shallow bank on the east side of the fjord.

The dispersion in both regions is inhomogeneous. To illustrate this, we release one particle at each timestep (i.e. every 6 min.) from five different sources

(indicated in the upper panels of Figures 4 and 5 by the crosses). The lower panels in those figures show the particle positions after each particle has been advected six tidal cycles. Consider first the Garten - Storfosna region shown in Figure 4; the red and black sources are in locations with strong currents and significant lateral shear, the purple and indigo sources have more uniform currents, while the blue sources are in relatively weak regions. As expected, the red and black particles spread over a larger area, about 10 km in both north-south and east-west directions. Interestingly they do not spread out uniformly but spread rather in distinct bands. The purple and indigo particles exhibit similar bandedness but spread only over 3-4 km. The blue particles essentially follow elliptical paths and remain near their starting locations. The inner fjord region experience similar inhomogeneous dispersion properties, see Figure 5.

For the statistical measures, it is preferable to have an array of particles deployed simultaneously. So we placed one particle in each grid cell (separated by 50 m) over both of the sub-regions. This yielded $25,600$ particles in each area. The particles were then advected forward for 10 tidal cycles.

Consider the averaged statistics first. The curves for the mean absolute dispersion (defined in 5) are shown in Figure 6. In both regions the dispersion is growing, reflecting that the particles are drifting systematically from their starting locations. The Storfosna - Garten dispersion shows a periodic collapse of the variance at the end of each cycle, due to the (incomplete) return journey to the starting locations. This oscillation is less pronounced at the inner fjord site, suggesting a more disordered spreading.

Interestingly, the dispersion does not asymptote to a linear growth regime (section 3.1) in either location. Both curves instead are *subdiffusive*, with $D^2 \propto t^{0.42}$ in the mouth of Trondheimsfjorden and $D^2 \propto t^{0.29}$ in the Storfosna - Garten region. The possible causes for this are discussed below.

The relative dispersion in the Storfosna - Garten area is shown in Figures 7 and 8. The former shows the early growth while the latter shows the late growth compared with the absolute dispersion. The early growth is nearly exponential, with an e-folding time of about one tidal cycle. This growth phase only persists for the first two cycles; thereafter the dispersion is slower than exponential. So the lateral spreading changes as the particles become more disordered. The dispersion after the second cycle (Figure 8) is closer to a power law dependence. The exponent, 0.74, is somewhat more than twice the exponent for the absolute dispersion (0.29). The relative dispersion is increasing toward the absolute dispersion but is still less. So the mean separation between particles is less than the mean separation between the individual particles and their starting positions.

As noted earlier, the limitation of mean statistics is that they involve averaging particles from different mixing regimes. The displacements of the red and black particles in Figures 4 and 5 are thus averaged together with those of the blue particles. An alternate approach is to map values obtained from single or two particle displacements back on to the initial field. Then "hot spots" can be differentiated from regions of weak mixing.

For example, Figure 9 shows the absolute dispersion as a function of (x,y) for the particles in the Storfosna - Garten region, 1 and 3 tidal cycles after the initial deployment. As expected, the fields are not at all homogeneous but exhibit bands of strongly localized advection separated by regions of very weak advection. The largest dispersion occurs near land, not in the strong current regions between the two promontories. The dispersion also depends on *when* the particles are deployed. The spatial dependence of the dispersion for particles deployed during the ebb tide (upper panels) differs remarkably from that for particles deployed during the flood (lower panels).

A more refined picture of the straining is obtained by mapping the relative dispersion (Figure 10). This reflects the separation of adjacent particles and thus not necessarily large (single particle) displacements. In line with this, the largest separations occur on the boundaries between regions of strong and weak absolute dispersion, rather than in the middle of regions of large absolute dispersion. These boundaries have a distinct filamentary appearance. Moreover, the filaments spread out, filling the domain after successive cycles.

The DLE presents a very similar picture of the straining as the relative dispersion. To calculate the DLE, we apply equation (9) to produce a square matrix of DLE values, which we then contour in Figure 11. As with the relative dispersion, the DLE indicates the straining occurs primarily along distinct material surfaces which emanate from the coastal promontories, and then spread into the interior with successive tidal cycles. Figure 12 shows the DLE values for the inner fjord region.

If pairs are separating exponentially along the material surfaces, the value of the DLE reflects the e-folding time for the growth in separation. The maximum values in the Storfosna - Garten region after 1 tidal cycle are near 0.4. From the mean relative dispersion, we inferred an e-folding time scale of about one day. Since the latter pertains to *square* separations, the implied growth rate for separations is about 0.5, similar to the maximum DLE. So the mean relative dispersion evidently *reflects the maximum rate of separation* occurring in the region. Note too that the maximum DLE after 3 tidal cycles is about three times less than after 1 cycle; this is because the third cycle is after the period of exponential growth. So the DLE should be decreasing with time.

Lastly we consider what happens when additional tidal components are added. [3] The next most energetic component is the S_2, which is roughly 35 % as strong as the M_2. Adding the S_2 alters the dispersion very little. This can be seen for example in the mean relative dispersion, shown in Figure 13. The dispersion with $M_2 + S_2$ is somewhat greater than with M_2 alone. The reason for this is that the S_2 during this period is in phase with the M_2, and therefore increases the amplitude of the particle displacements. The change however is relatively minor. In other periods, when the S_2 is out of phase, the $M_2 + S_2$ is less.

Potentially more interesting is the dispersion with the addition of the K_1. Since the S_2 has the same time dependence as the M_2, it is less surprising that S_2 acts primarily to change the amplitude. The K_1 however has a different frequency, and superimposing perturbations with different time dependencies can enhance chaotic mixing (e.g. Pierrehumbert, 1991). However, this addition also induces relatively minor changes. The K_1 is only about 10 % as strong as the M_2, and adding it causes a small decrease in the relative dispersion compared to that with M_2 alone. Evidently the K_1 would have to be stronger in relative terms to change the results.

5 Discussion

We have deployed particles in a numerical model to quantify the lateral mixing occurring in a tidally-driven fjord (Trondheimsleia and the Trondheims fjord in western Norway). The flow represents that arising from the dominant tidal components, the M_2, S_2 and also the K_1, without wind-driving.

We quantified the particle motion using various measures. The general picture which emerges is one of strongly inhomogeneous mixing, with the degree of straining depending both on the tracer's location and the time of its deployment in the tidal cycle. The specific findings were as follows:

- The absolute dispersion (the mean square displacement of particles from their starting positions) suggests the asymptotic mixing is significantly *sub-diffusive*, increasing somewhat slower than time to the first power. This perhaps reflects the coasts constraining lateral spreading; it also implies that one could not parameterize this tidal mixing as a simple diffusive process.
- The relative dispersion (the mean square separation of particle pairs) exhibits exponential growth during the first 1-2 tidal cycles, with an e-folding

[3] While the 50 m simulations were only run for the M_2 tide, additional components were simulated on a 100 m grid. However the Lagrangian dispersion due to the M_2 with 100 m resolution was nearly the same as with 50 m resolution. So using the 100 m simulation for the following comparison is reasonable.

time of about one cycle. This is consistent with chaotic mixing. The late-time growth had a power law dependence on time, but was sub-diffusive,like the absolute dispersion.

- Contouring the absolute dispersion as a function of space revealed adjacent regions of large and small particle drift. Contouring the relative dispersion this way suggested the straining between particles was greatest on the boundaries between these regions, on distinct material surfaces.
- The Direct Lyapunov Exponent revealed much the same structure as the relative dispersion, with heightened straining occurring on material surfaces. The exponential growth rate inferred from the mean relative dispersion was comparable to the *maximum* DLE values after the first tidal cycle. So mean relative dispersion evidently reflects the maximum straining occurring.

The straining in the two regions examined is dominated by the M_2 tide. Adding additional semi-diurnal components only modified the amplitude of the dispersion without significantly altering its spatial characteristics or its temporal growth. Adding the K_1 tide similarly did not affect the mean dispersion; however this is perhaps not surprising, given that the amplitude of the K_1 is only about 1/10th that of the M_2.

The present model lacks both wind-forcing and nonlinear effects, and both could conceivably alter the mixing properties. Both can produce lower frequency fluctuations which could augment the particle drift induced by the M_2. We are in the process of including momentum advection into the tidal code, and we will be able to test the modifications thereafter. Likewise, we will implement wind forcing later on and evaluate that as well. But we emphasize that the Lagrangian methods discussed in this work are applicable with more complete models; so we would be able to compare later results directly with those discussed here.

As noted, the mean absolute and relative dispersion present an ensemble picture of the particle spreading and miss the inhomogeneities revealed by the mappings. But the mean measures nevertheless provide useful information about the *temporal* variations in the mixing. The relative dispersion exhibits two phases, an early exponential growth and a later power-law growth, and this could not have been inferred from two snapshots of the DLE. In addition, the DLE produced a field very similar to that from the mapped relative dispersion, which is easier to calculate. The DLE does reflect the growth rate, *assuming* exponential growth is occurring. But we feel in any case that it should be used in conjunction with the other measures, such as the mean dispersions. More advanced methods exist as well (Malhotra and Wiggins, 1998; Haller and Yuan, 2000), but these are unlikely to yield drastic changes from the picture inferred here.

These Lagrangian measures would be of great value for applications in the

fjord. For example, a sewer outflow pipe would best be located near a region of strong lateral shearing, to hasten lateral mixing. The promontories in the Storfosna - Garten section are such regions. And large relative dispersion in a region implies a sensitive dependence of trajectories on the particle's initial location. Knowing this will impact search and rescue operations.

6 Discussion

We have deployed particles in a numerical model to quantify the lateral mixing occurring in a tidally-driven fjord (Trondheimsleia and the Trondheims fjord in western Norway). The flow represents that arising from the dominant tidal components, the M_2, S_2 and also the K_1, without wind-driving.

We quantified the particle motion using various measures. The general picture which emerges is one of strongly inhomogeneous mixing, with the degree of straining depending both on the tracer's location and the time of its deployment in the tidal cycle. The specific findings were as follows:

- The absolute dispersion (the mean square displacement of particles from their starting positions) suggests the asymptotic mixing is significantly *sub-diffusive*, increasing somewhat slower than time to the first power. This perhaps reflects the coasts constraining lateral spreading; it also implies that one could not parameterize this tidal mixing as a simple diffusive process.
- The relative dispersion (the mean square separation of particle pairs) exhibits exponential growth during the first 1-2 tidal cycles, with an e-folding time of about one cycle. This is consistent with chaotic mixing. The late-time growth had a power law dependence on time, but was sub-diffusive,like the absolute dispersion.
- Contouring the absolute dispersion as a function of space revealed adjacent regions of large and small particle drift. Contouring the relative dispersion this way suggested the straining between particles was greatest on the boundaries between these regions, on distinct material surfaces.
- The Direct Lyapunov Exponent revealed much the same structure as the relative dispersion, with heightened straining occurring on material surfaces. The exponential growth rate inferred from the mean relative dispersion was comparable to the *maximum* DLE values after the first tidal cycle. So mean relative dispersion evidently reflects the maximum straining occurring.

The straining in the two regions examined is dominated by the M_2 tide. Adding additional semi-diurnal components only modified the amplitude of the dispersion without significantly altering its spatial characteristics or its temporal growth. Adding the K_1 tide similarly did not affect the mean dispersion; however this is perhaps not surprising, given that the amplitude of the K_1 is only

about 1/10th that of the M_2.

The present model lacks both wind-forcing and nonlinear effects, and both could conceivably alter the mixing properties. Both can produce lower frequency fluctuations which could augment the particle drift induced by the M_2. We are in the process of including momentum advection into the tidal code, and we will be able to test the modifications thereafter. Likewise, we will implement wind forcing later on and evaluate that as well. But we emphasize that the Lagrangian methods discussed in this work are applicable with more complete models; so we would be able to compare later results directly with those discussed here.

As noted, the mean absolute and relative dispersion present an ensemble picture of the particle spreading and miss the inhomogeneities revealed by the mappings. But the mean measures nevertheless provide useful information about the *temporal* variations in the mixing. The mean relative dispersion exhibits two phases, an early exponential growth and a later power-law growth, and this could not have been inferred from contour-plots of the relative dispersion or the DLE. The DLE does reflect the growth rate, *assuming* exponential growth is occurring. But we feel in any case that it should be used in conjunction with the other measures, such as the mean dispersions. More advanced methods exist as well (Malhotra and Wiggins, 1998; Haller and Yuan, 2000), but these are unlikely to yield drastic changes from the picture inferred here.

These Lagrangian measures would be of great value for applications in the fjord. Pathogen spreading from salmon farms is one example of a potential threat carried by coastal mixing. Information on which area that experiences the most rapid mixing is therefore of great interest. A sewer outflow pipe would best be located near a region of strong lateral shearing, to hasten lateral mixing. The promontories in the Storfosna - Garten section are such regions. And large relative dispersion in a region implies a sensitive dependence of trajectories on the particle's initial location. Knowing this will impact search and rescue operations.

Acknowledgements

Steinar Orre would like to thank Atle Ommundsen for useful guidance at an early stage of this study.

Joseph H. LaCasce was supported under the Norwegian NOCLIM II program.

References

Aref, H., 1984. Stirring by chaotic advection. Journal of Fluid Mechanics 143, 1–21.

Batchelor, G. K., 1953. The Theory of Homogeneous Turbulence. Cambridge University Press.

Bennett, A. F., 1987. A Lagrangian analysis of turbulent diffusion. Rev. of Geophys 25 (4), 799–822.

Bowden, K. F., 1965. Horizontal mixing in the sea due to a shearing. Journal of Fluid Mechanics 21, 83–95.

Forrest, M. H., Usseglio-Polatera, J., 1984. Dispersion simulation in two-dimensional tidal flow. Journal of Hydraulic Engineering 110, 905–926.

Geyer, R. W., Signell, R. P., 1992. A reassessment of the role of tidal dispersion in estauries and bays. Estauries 15, 97–108.

Gjevik, B., 1996. Models of drift and dispersion in tidal flows. J. Grue et al. (eds.), Kleuwer Academic Publishers, Ch. 2, pp. 343–354.

Gjevik, B., Hareide, D., Lynge, B., Ommundsen, A., Skailand, J., Urheim, H., 2005. Implementation of high resolution tidal current fields in electronic charts systems. Journal of Marine Geodesy (in press).

Haller, G., 2001. Distinguished material surfaces and coherent structure in three-dimensional fluid flows. Physica D 49, 248–277.

Haller, G., Yuan, G., 2000. Lagrangian coherent structures and mixing in two-dimensional turbulence. Physica D 147, 352–370.

Haynes, P., 2005. Stratospheric dynamics. Ann. Rev. Fluid Mech. 37, 263–93.

LaCasce, J., 2005. Lagrangian statistics from oceanic and atmospheric observations. Springer-Verlag.

LaCasce, J., Ohlmann, C., 2003. Relative dispersion at the surface of the Gulf of Mexico. Journal of Marine Research 61, 285–312.

Lapeyre, G., 2002. Characterization of finite time Lyapunov exponents and vectors in two-dimensional turbulence. Chaos 12, 688–698.

Malhotra, N., Wiggins, S., 1998. Geometric Structures, Lobe Dynamics, and Lagrangian Transport in Flows with Aperiodic Time-Dependence, with Application to Rossby Wave Flow. Journal of Nonlinear Science 8, 401–456.

Miller, P., Jones, C., Rogerson, A., Pratt, L., 1997. Quantifying transport in numerically-generated velocity fields. Physica D 110, 105–122.

Miller, P., Pratt, L., K.R., H., Jones, C., 2002. Chaotic transport of mass and potential vorticity for an island recirculation. J. Phys. Oceanogr. 32, 80–102.

Moe, H., Gjevik, B., Ommundsen, A., 2003. A high resolution tidal model for the coast of møre and trøndelag, mid norway. Norwegian Journal of Geography 57, 65–82.

Ommundsen, A., 2002. Models of cross shelf transport introduced by the Lofoten Maelstrom. Continental Shelf Research 22, 93–113.

Orre, S., 2004. Kaotisk transport og miksing i kystnaere tidevannsfelt. Master's thesis, Department of Mathematics, University of Oslo.

Ottino, J., 1990. The kinematics of mixing. Cambridge University Press.

Pierrehumbert, R. T., 1991. Chaotic Mixing of Tracer and Vorticity by Modulated Traveling Rossby Waves. Geophysical and Astrophysical Fluid Dynamics 58, 285–320.

Ridderinkhof, H., Loder, J. W., 1994. Lagrangian characterization of circulation over submarine banks with application to the outer Gulf of Maine. Journal of Physical Oceanography 24, 1184–1200.

Ridderinkhof, H., Zimmerman, J., 1992. Chaotic stirring in a tidal system. Science 258, 1107–1111.

Rogerson, A., Miller, P., Pratt, L., Jones, C., 1999. Lagrangian motion and fluid exchange in a Barotropic Meandering Jet. Journal of Physical Oceanography 29, 2635–2655.

Sawford, B. L., 2001. Turbulent relative dispersion. Annual Review of Fluid Mechanics 33, 289–317.

Shepherd, T., Koshyk, J., Ngan, K., 2000. On the nature of large-scale mixing in the stratosphere and mesosphere. Journal of Geophysical Research 105, 12433–12446.

Signell, R. P., Butman, B., 1992. Modeling tidal exchange and dispersion in Boston Harbor. Geophysical Research Letters 97, 15591–15606.

Signell, R. P., Geyer, R., 1991. Transient eddy formation in and around headlands. Journal of Geophysical Research 96, 2561–2575.

Solomon, T. H., Weeks, E. R., Swinney, H. L., 1993. Observation of anomalous diffusion and Levy flights in a two-dimensional rotating flow. Physical Review Letters 71, 3975–3978.

Taylor, G. I., 1921. Diffusion by continuous movements. Proc. London Math. Soc.

Vetterling, W. T., Flannery, B. P., 2002. Numerical recepies in C++. Cambridge University Press.

Wiggins, S., 1992. Chaotic Transport in Dynamical Systems. Springer-Verlag.

Wiggins, S., 2005. The Dynamical Systems approach to Lagrangian Transport in Oceanic Flows. Ann. Rev. Fluid Mech. 37, 295–328.

Young, W. R., 1999. Lectures on Stirring and Mixing. In: Proceedings of the Woods Hole Summer Program in Geophysical Fluid Dynamics. `www-pord.ucsd.edu/~wryoung/`.

List of Figures

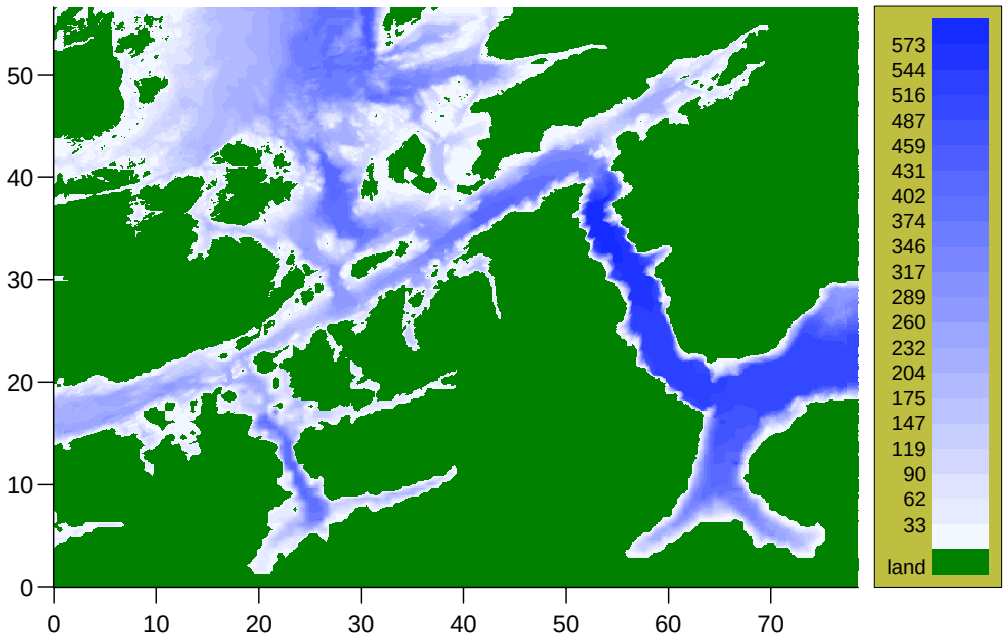

Fig. 1. Model domain with 50 m grid resolution. $x-$ and $y-$axis are given in kilometres, color depth-scale in metres.

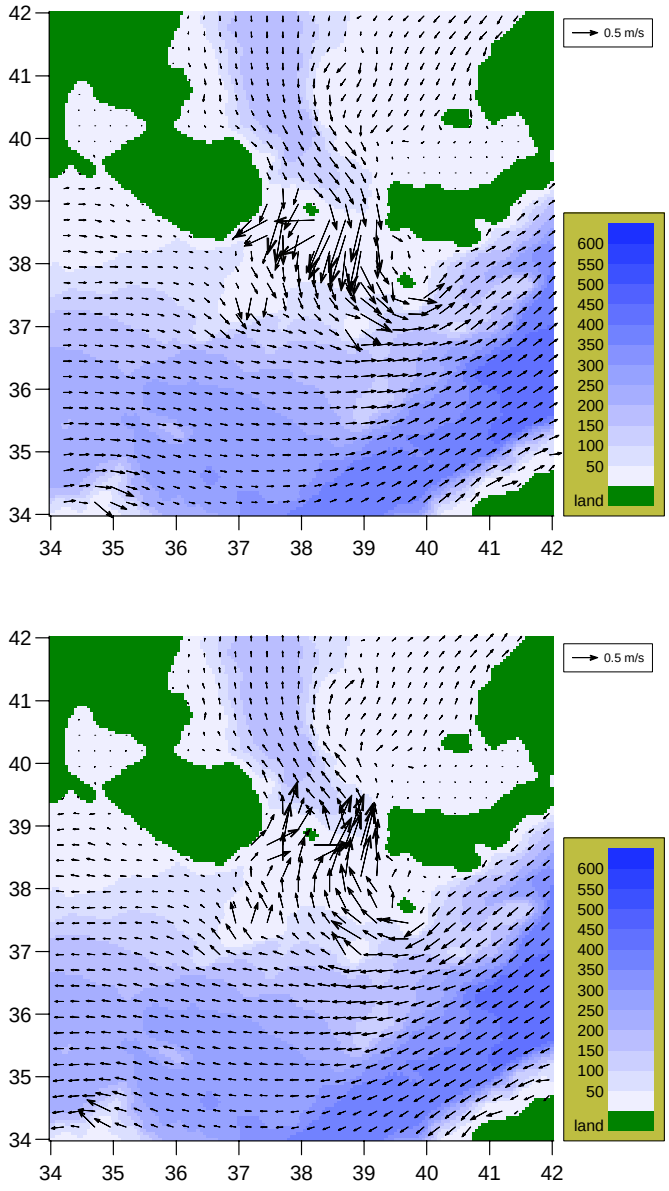

Fig. 2. Current velocity field for the tidal component M_2 in the Storfosna - Garten area, left figure shows maximum southward currents, right figure shows maximum northward currents 6.2 hours later. $x-$ and $y-$axis are given in kilometres, depth-scale in metres.

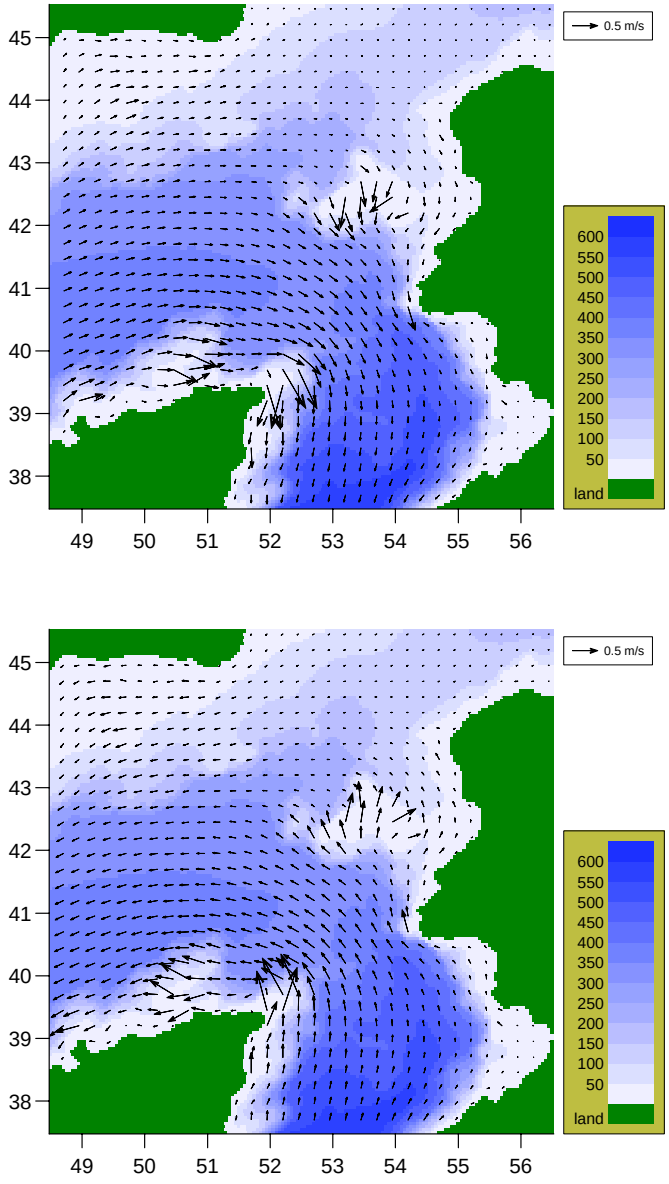

Fig. 3. Current velocity field for the tidal component M_2 at the mouth of Tronheimsfjorden, left figure shows maximum southward currents, right figure shows maximum northward currents 6.2 hours later. $x-$ and $y-$axis are given in kilometres, depth-scale in metres.

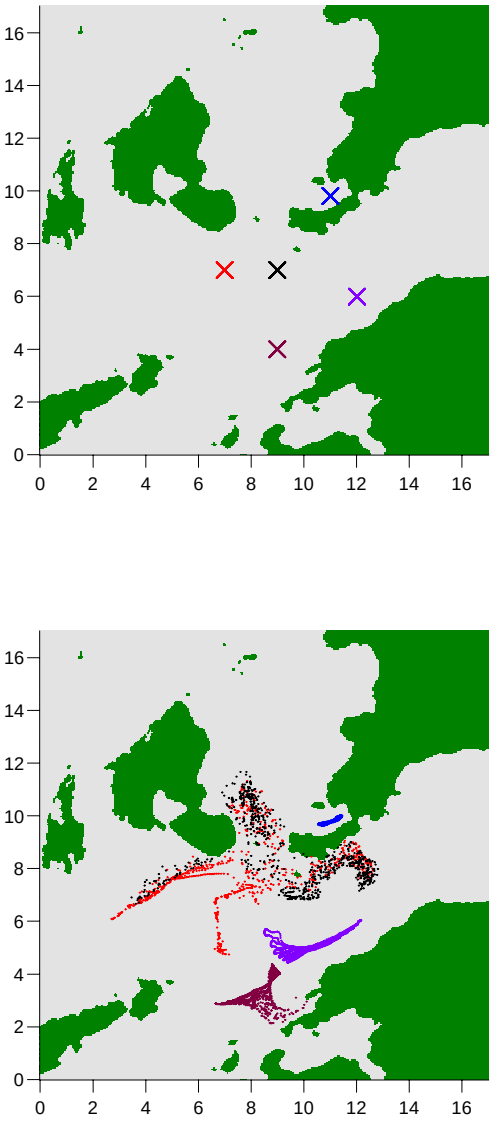

Fig. 4. Five selected sources for continuous releases of Lagrangian particles in the Sorfosna - Garten area. The right figure shows the spreading after 6 tidal cycles (74 hours) with the M_2 constituent. $x-$ and $y-$axis are given in kilometres.

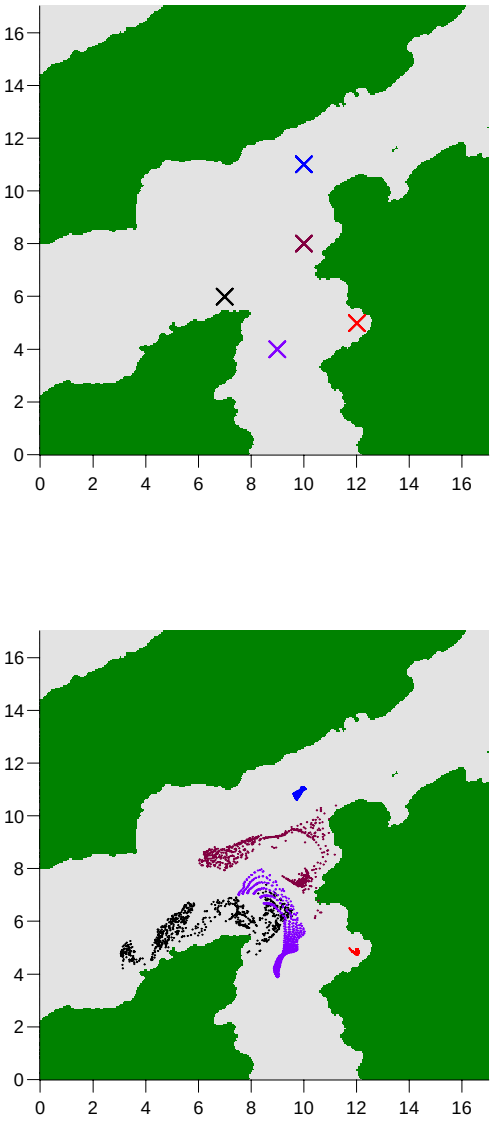

Fig. 5. Five selected sources for continuous releases of Lagrangian particles at the mouth of Trondheimsfjorden. The right figure shows the spreading after 6 tidal cycles (74 hours) with the M_2 constituent. $x-$ and $y-$axis are given in kilometres.

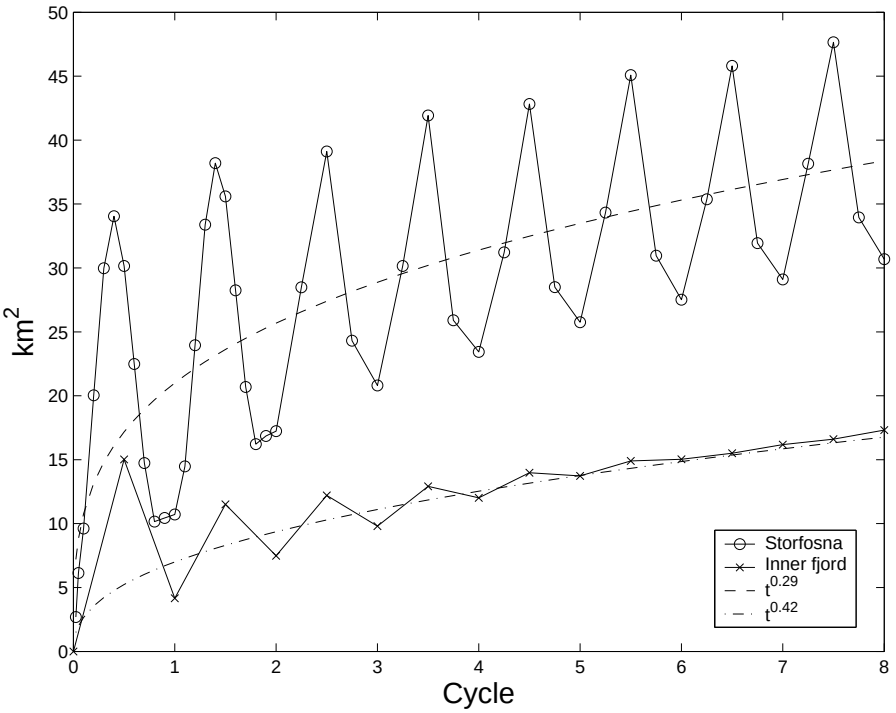

Fig. 6. Mean absolute dispersion from the two locations in Trondheimsleia over eight tidal cycles, the Storfosna - Garten area depicted with circles and the inner fjord with x-marks.

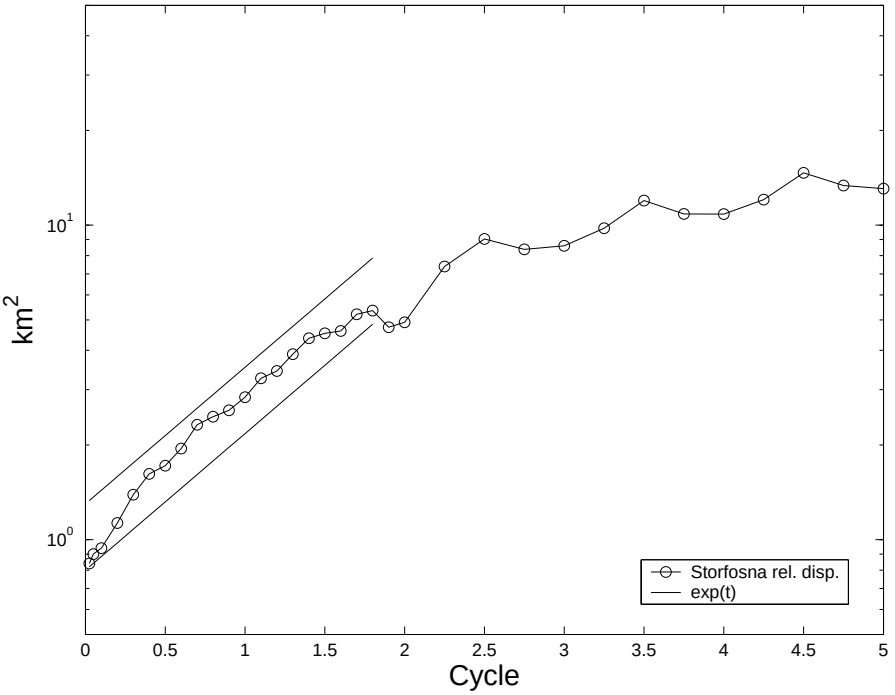

Fig. 7. Mean relative dispersion from the Storfosna - Garten area over the first five tidal cycles.

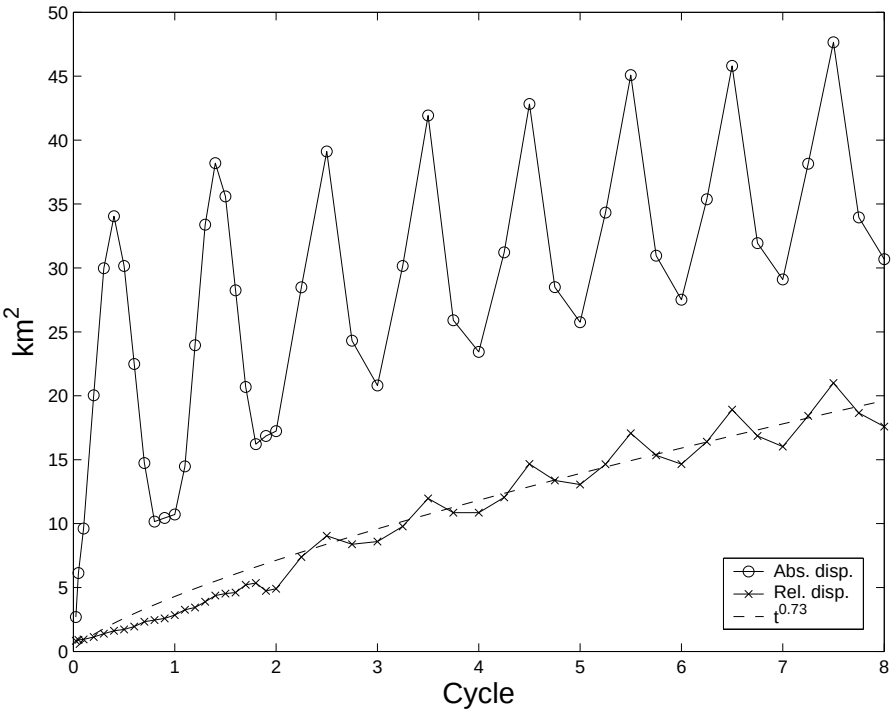

Fig. 8. Mean relative dispersion and mean absolute dispersion from the Storfosna - Garten area over eight tidal cycles.

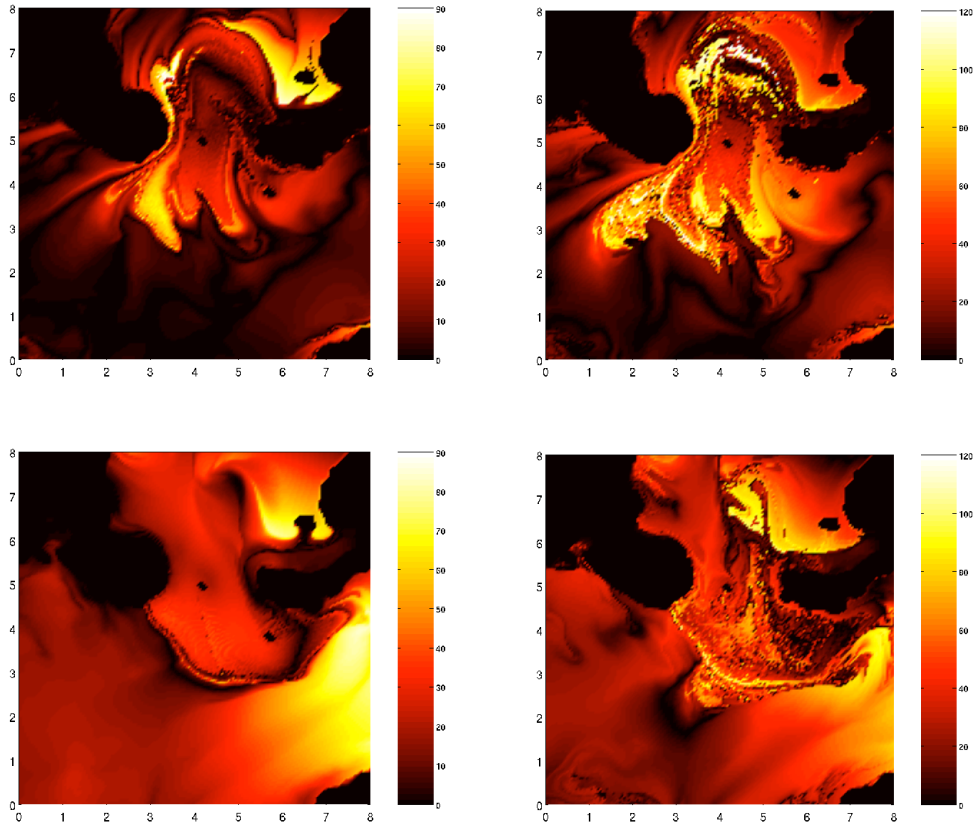

Fig. 9. Contour plot of D^2 values after 1 (left) and 3 (right) tidal cycles for the Storfosna - Garten area. Upper panel differ from the lower panel by half a tidal cycle phase shift in the starting point. $x-$ and $y-$axis are given in kilometres, color depth-scale in km^2.

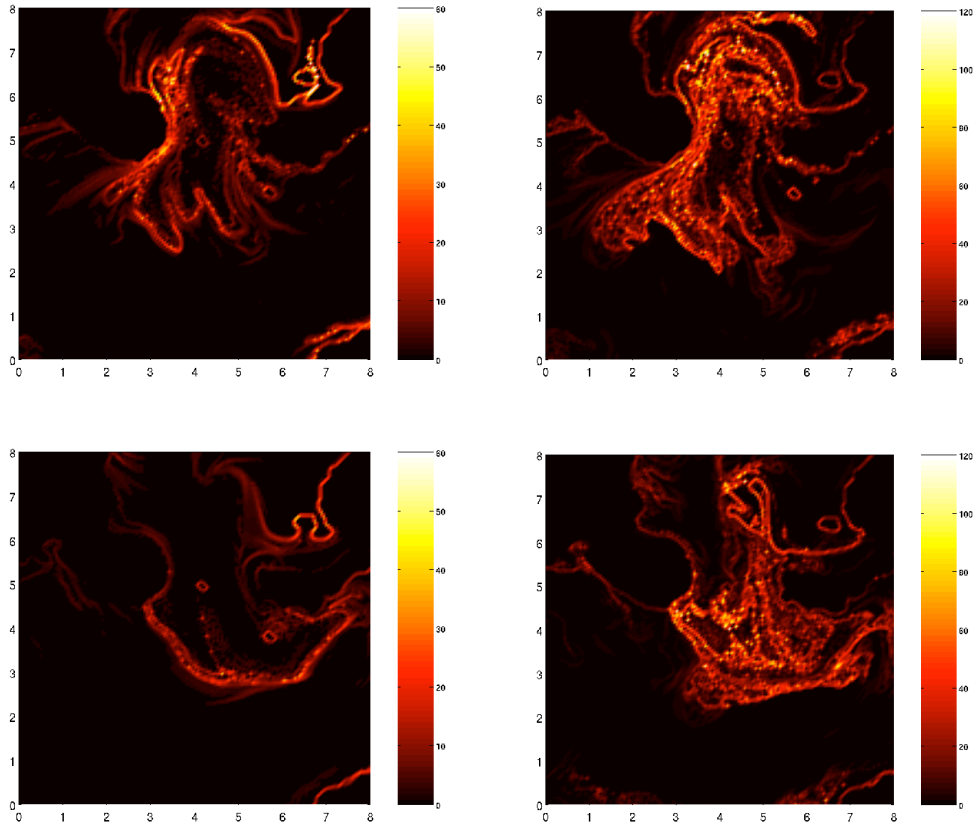

Fig. 10. Contour plot of R^2 values after 1 (left) and 3 (right) tidal cycles for the Storfosna - Garten area. Upper panel differ from the lower panel by half a tidal cycle phase shift in the starting point. $x-$ and $y-$axis are given in kilometres, color depth-scale in km^2.

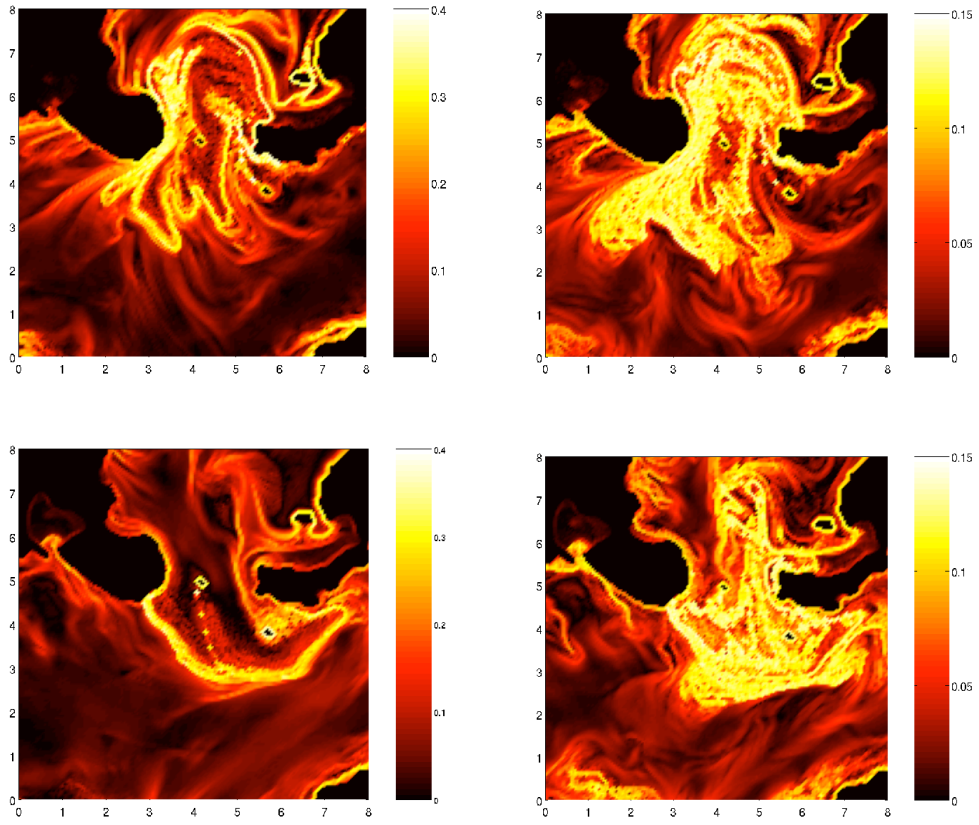

Fig. 11. Contour plot of DLE values after 1 (left) and 3 (right) tidal cycles for the Storfosna - Garten area. Upper panel differ from the lower panel by half a tidal cycle phase shift in the starting point. $x-$ and $y-$axis are given in kilometres, color depth-scale in hour^{-1}.

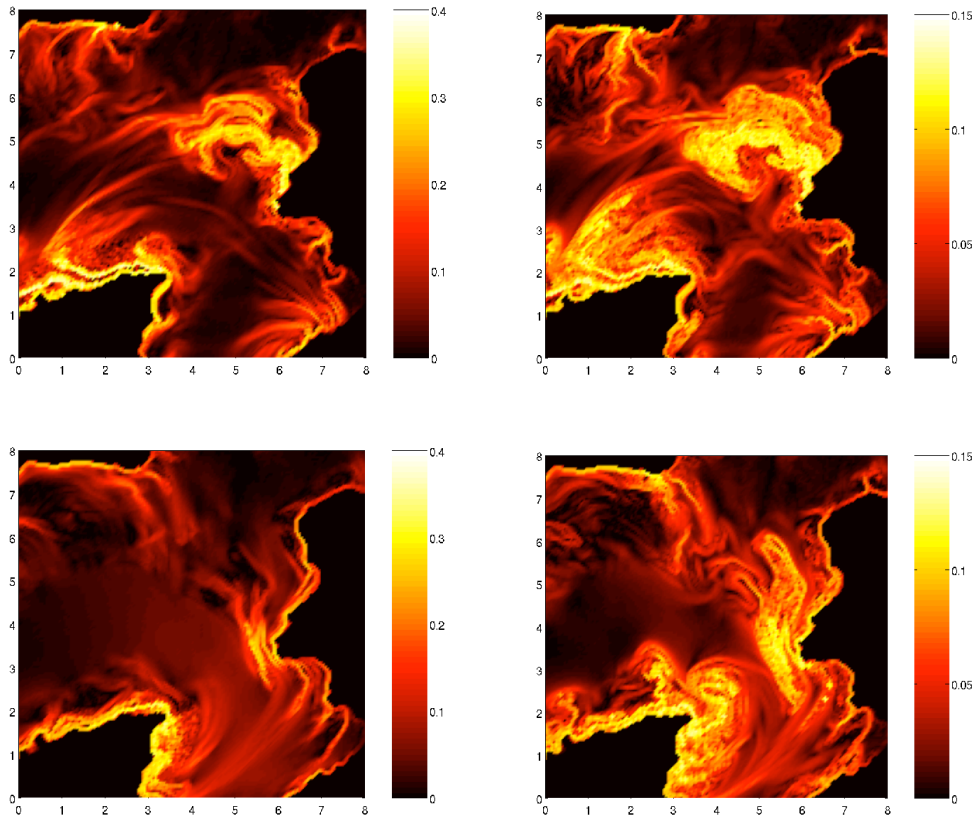

Fig. 12. Contour plot of DLE values after 1 (left) and 3 (right) tidal cycles at the mouth of Trondheimsfjorden. Upper panel differ from the lower panel by half a tidal cycle phase shift in the starting point. $x-$ and $y-$axis are given in kilometres, color depth-scale in hour^{-1}.

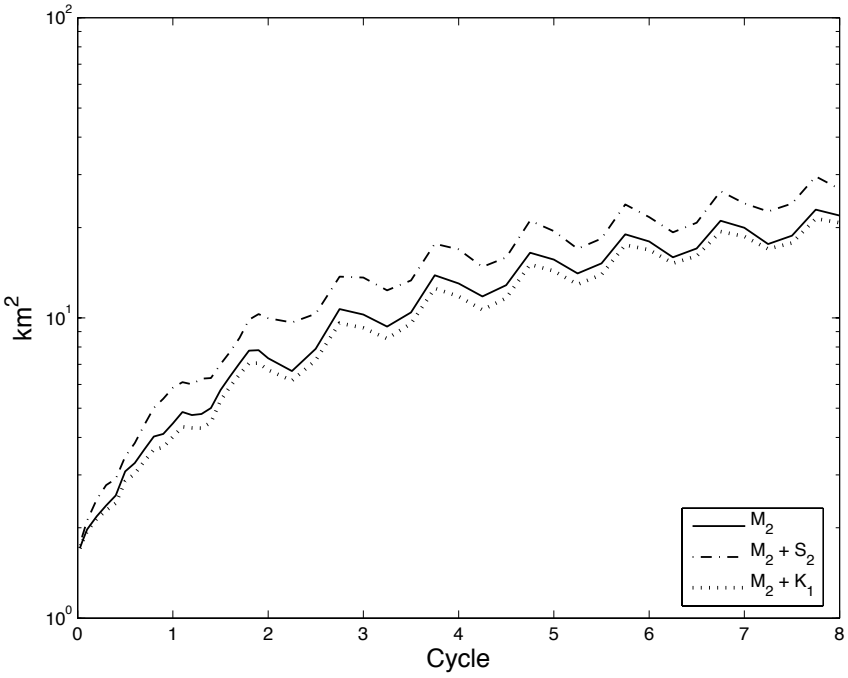

Fig. 13. Mean relative dispersion from the Storfosna - Garten area over eight tidal cycles, with the additional tidal components S_2 and K_1.